



Highly multiplexed single-cell analysis of formalin-fixed, paraffin-embedded cancer tissue

Michael J. Gerdes^{a,1}, Christopher J. Sevinsky^{b,1}, Anup Sood^{c,1}, Sudeshna Adak^d, Musodiq O. Bello^{e,2}, Alexander Bordwell^{c,3}, Ali Can^e, Alex Corwin^f, Sean Dinn^c, Robert J. Filkins^g, Denise Hollman^{b,3}, Vidya Kamath^h, Sireesha Kaanumalle^c, Kevin Kennyⁱ, Melinda Larsen^{a,4}, Michael Lazare^{i,3}, Qing Li^j, Christina Lowes^j, Colin C. McCulloch^k, Elizabeth McDonough^j, Michael C. Montalto^{l,5}, Zhengyu Pang^b, Jens Rittscher^m, Alberto Santamaria-Pang^e, Brion D. Sarachanⁿ, Maximilian L. Seel^b, Antti Seppo^a, Kashan Shaikh^f, Yunxia Sui^k, Jingyu Zhang^b, and Fiona Ginty^{o,6}

^aCell Biology Laboratory, ^bBiochemistry and Bioanalytics Laboratory, ^cBiological and Organic Chemistry Laboratory, ^dBiomedical Image Analysis Laboratory, ^eMicro-System and Micro-Fluidics Laboratory, ^fClinical Systems and Signal Processing Organization, ^gComputational Biology and Biostatistics Laboratory, ^hAdvanced Computing Laboratory, ⁱBiomedical Imaging and Physiology Laboratory, ^jApplied Statistics Laboratory, ^kMolecular Imaging and Diagnostics Advanced Technologies, ^lComputer Vision Laboratory, ^mSoftware Science and Analytics Organization, and ⁿLife Sciences and Molecular Diagnostics Laboratory, GE Global Research Center, Niskayuna, NY 12309; and ^oGE Healthcare, John F. Welch Technology Centre, 560066 Bangalore, India

Edited by Dennis A. Carson, University of California, San Diego, La Jolla, CA, and approved May 15, 2013 (received for review January 4, 2013)

Limitations on the number of unique protein and DNA molecules that can be characterized microscopically in a single tissue specimen impede advances in understanding the biological basis of health and disease. Here we present a multiplexed fluorescence microscopy method (MxIF) for quantitative, single-cell, and subcellular characterization of multiple analytes in formalin-fixed paraffin-embedded tissue. Chemical inactivation of fluorescent dyes after each image acquisition round allows reuse of common dyes in iterative staining and imaging cycles. The mild inactivation chemistry is compatible with total and phosphoprotein detection, as well as DNA FISH. Accurate computational registration of sequential images is achieved by aligning nuclear counterstain-derived fiducial points. Individual cells, plasma membrane, cytoplasm, nucleus, tumor, and stromal regions are segmented to achieve cellular and subcellular quantification of multiplexed targets. In a comparison of pathologist scoring of diaminobenzidine staining of serial sections and automated MxIF scoring of a single section, human epidermal growth factor receptor 2, estrogen receptor, p53, and androgen receptor staining by diaminobenzidine and MxIF methods yielded similar results. Single-cell staining patterns of 61 protein antigens by MxIF in 747 colorectal cancer subjects reveals extensive tumor heterogeneity, and cluster analysis of divergent signaling through ERK1/2, S6 kinase 1, and 4E binding protein 1 provides insights into the spatial organization of mechanistic target of rapamycin and MAPK signal transduction. Our results suggest MxIF should be broadly applicable to problems in the fields of basic biological research, drug discovery and development, and clinical diagnostics.

cancer diagnostics | high-content cellular analysis | image analysis | mTOR | multiplexing

Advances in molecular characterization technologies have radically affected cancer research, understanding, diagnosis, and treatment. For example, comprehensive genomic analysis shows that breast cancer can be divided into at least four intrinsic molecular subtypes, and each subtype is associated with a differential phenotype, prognosis, and response to therapy (1, 2). Comprehensive molecular profiling has also revealed intrinsic molecular subtypes of other cancers, including glioblastoma, squamous lung, colorectal, and ovarian cancers (3–6). These classifications promise to drive development of new diagnostics and inform therapy decisions. Although multigene-based tests facilitate interrogation of broad genomic profiles of the whole specimen, important histological, cellular, and subcellular context is lost. Continued advances in basic and translational cancer research will likely require new comprehensive molecular profiling technologies.

Motivated by the need to maximize biomarker data from costly drug discovery efforts and clinical trials, shrinking sample

sizes, and increasing appreciation of disease complexity, the use of multiplexed molecular analysis has steadily increased (7). Formalin-fixed paraffin-embedded (FFPE) tissue is the most common form of preserved archived clinical sample. FFPE tissues are extensively used for routine diagnosis, and archived, clinically annotated FFPE specimens have been used successfully to identify prognostic and predictive cancer biomarkers in retrospective analyses (8–10). Chromogenic immunohistochemistry (IHC) is commonly used to determine in situ biomarker expression in FFPE tissue [e.g., diaminobenzidine (DAB) staining] but suffers from a number of inherent limitations, including the requirement of a new sample for each analyte, nonlinear staining intensity, and laboratory-to-laboratory variability due to subjective semiquantitative analysis (11).

Fluorescence microscopy enables limited multiplexed, quantitative analyses in cell and tissue specimens. Up to five fluorescent dyes can be spectrally resolved using standard optical filters, and separation of up to seven fluorophores has been reported with multispectral imaging (12). Despite these attributes, intrinsic autofluorescence often precludes detection of all but the most abundant molecules in fluorescence microscopy of FFPE tissues (13).

The limitations described above motivated us to develop an analytical technology capable of quantitative, high-dimensional, in situ data acquisition from biological tissue specimens (Fig. 1). In this report we describe a fluorescence microscopy procedure that enables high-level multiplexing of protein and nucleic acid detection

Author contributions: M.J.G., C.J.S., A. Sood, R.J.F., M.C.M., A.S.-P., B.D.S., and F.G. designed research; M.J.G., C.J.S., A. Sood, M.O.B., A.B., A. Can, S.D., D.H., S.K., K.K., M. Larsen, M. Lazare, Q.L., C.L., C.C.M., E.M., Z.P., A.S.-P., M.L.S., A. Seppo, and J.Z. performed research; M.J.G., C.J.S., A. Sood, M.O.B., A. Can, A. Corwin, S.D., R.J.F., V.K., K.K., C.C.M., Z.P., J.R., A.S.-P., B.D.S., K.S., Y.S., and F.G. contributed new reagents/analytic tools; M.J.G., C.J.S., A. Sood, S.A., Q.L., Z.P., Y.S., and F.G. analyzed data; and M.J.G., C.J.S., A. Sood, and F.G. wrote the paper.

Conflict of interest statement: All authors affiliated with GE Global Research Center, Niskayuna, NY, 12309 are current employees of General Electric Company.

This article is a PNAS Direct Submission.

Freely available online through the PNAS open access option.

¹M.J.G., C.J.S., and A. Sood contributed equally to this work.

²Present address: Clinical Software Engineering, GE Healthcare Waukesha, WI 53188.

³Present address: MultiOmyx R&D Laboratory, Clariant: A GE Healthcare Company, Aliso Viejo, CA 92656.

⁴Department of Biological Sciences, State University of New York at Albany, Albany, NY 12222.

⁵Clinical and Medical Affairs Omnyx, LLC, Pittsburgh, PA 15212.

⁶To whom correspondence should be addressed. E-mail: ginty@research.ge.com.

This article contains supporting information online at www.pnas.org/lookup/suppl/doi:10.1073/pnas.1300136110/-DCSupplemental.

and quantitation in a single FFPE tissue section. Image-processing algorithms register image stacks, remove intrinsic autofluorescence, segment individual cells and tissue compartments, and quantify subcellular expression levels of multiplexed molecular targets. We report several aspects of this technology, including combined immunofluorescence, H&E, and DNA FISH, a comparison of automated staining analysis to standard IHC in breast cancer, and single-cell analysis of 61 protein antigens in 747 human colorectal cancer specimens.

Results

Development of a Fluorophore Inactivation Solution. Because fluorescence analytical approaches limit the number of target measurements possible in a single tissue specimen, we developed an assay capable of exceeding these limits in multiple sample types, including FFPE tissues. Alkaline oxidation chemistry was developed that eliminates cyanine-based dye fluorescence within 15 min (U.S. patent 7,741,045) (14). The kinetics of fluorescence inactivation was measured via changes in optical absorbance (Fig. S1). After 5 min in dye inactivation solution, 60% and 80% reductions in absorbance were observed for Cy3 and Cy5, respectively (Fig. S1A and B). A 15-min reaction with inactivation solution was sufficient to reduce fluorescence signals to less than 2% of original intensities. In corresponding control experiments, dyes showed no loss of absorption in PBS, and absorbance measurements of inactivated dyes returned to PBS confirmed the reaction is irreversible (Fig. S2). Additional fluorescent dyes were also evaluated (Fig. S1C). Unlike Cy dyes, absorbance spectra of DAPI, fluorescein (FITC), and ATTO495 remained unchanged after 30-min reactions with inactivation solution. Given DAPI's utility as a nuclear counterstain, we explored this finding further. DAPI's absorbance spectrum remained unchanged in 140-min reactions with the inactivation solution (Fig. S1D). Therefore, DAPI-stained nuclei can be imaged in each staining round and used as spatial reference points for registration, enabling quantitative analysis of image stacks (Figs. S3 and S4).

Sample Preparation and Dye-Cycling Conditions. We devised a routine process for sample analysis. Tissue was dewaxed and rehydrated using standard conditions, followed by a two-step antigen retrieval process that allows for application of antibodies that work optimally with acidic, basic, or protease-based antigen retrieval (U.S. patent 8,067,241) (15).

To address the possibility that dye inactivation would result in loss of target epitopes and/or tissue integrity, we examined four markers with distinct subcellular localization patterns after repeated dye-inactivation reactions. Cyanine 3 (Cy3)-labeled anti- β -catenin and cyanine 5 (Cy5)-labeled anti- α smooth muscle actin (SMA) were analyzed in breast tissue over 100 reaction cycles, and Cy3-labeled anti-cellular tumor antigen p53 (p53) and Cy5-labeled anti-pan-keratin were analyzed in colon tissue over 90 reaction cycles. A sample was stained and imaged at each 10-cycle interval of repeated 15-min incubations in inactivation solution and compared with an untreated control. In both tissue specimens we observed no difference in staining intensity after all cycles for β -catenin and SMA and p53 and pan-keratin (Fig. S5D), confirming no loss of target antigens or tissue integrity.

In this report, staining of 72 antibody–antigen pairs is described. Of these, 59 have been tested in series of 0, 1, 5, and 10 dye-inactivation reactions as part of routine antibody–antigen characterization (Fig. S5A–C and Dataset S1); 51 were unaffected and 8 demonstrated some degree of sensitivity to the dye-inactivation chemistry. Seven of the eight were moderately affected and exhibited a lower signal intensity after one and five rounds of exposure, with staining still evident after 10 reactions. One target [ribosomal protein S6 (RPS6)] exhibited extreme sensitivity, with large decreases in staining intensity at one and five rounds, and almost complete elimination of signal by 10 rounds of dye inactivation.

No predictable trend based on cellular localization or phosphorylation status was evident in susceptible antigen–antibody pairs.

Single-Cell Analysis and Visualization of Biological Features. We stained lineage-specific proteins such as epithelial cytokeratins, endothelial CD31, and SMA to define cancer tissue's cellular makeup with cellular resolution (Fig. 2A and Fig. S6). Immunostains demarcating the plasma membrane, such as anti- Na^+K^+ ATPase, and DNA stains of the nucleus further enabled delineation of tissue and cellular architecture at single-cell and subcellular resolution (Figs. 1 and 2D and C). Pseudocolored, overlaid images were generated to visualize tissue architecture (Fig. 2E), and computational image analysis algorithms were used to generate segmentation masks for cellular and subcellular analysis of epithelial cells (16) (Figs. 1 and 2F).

We tested dye-cycling for compatibility with H&E staining of tissues at the end of the multiplexing cycle [eosin fluorescence precludes its use before multiplexed fluorescence microscopy (MxIF)]. DAPI images were computationally registered with hematoxylin-stained cell nuclei, allowing fluorescent images to be overlaid with the H&E image (Fig. S7) (17). Pseudocolored structural protein and DNA stains were also used to generate H&E-like images to aid in visualization and interpretation of tissue morphology (Figs. 2G and 3A, I). Chromogen-like pseudocoloring of single stains was used to facilitate staining interpretation in a manner consistent with traditional DAB staining (Fig. 2H).

Combined Immunofluorescence and DNA FISH. Combined analysis of nucleic acids and proteins from the same biological sample is of increasing importance in disease diagnosis (18). To test the utility of our dye-cycling method in combined analysis, breast cancer tissue samples were immunostained for human epidermal growth factor receptor 2 (HER2) and pan-keratin proteins, followed by DNA FISH analysis of the *HER2* gene. Tissue was probed with dye-labeled Cy5–anti-Her2 and Cy3–anti-pan-keratin antibodies and counterstained with DAPI (Fig. 2I). After dye inactivation, tissues were protease-treated followed by hybridization of dye-conjugated FISH probes for the *HER2* gene and centromere 17 (CEP17) as a reference marker. As expected, the CEP17 FISH probe produced two copies per nucleus in a majority of cells, and *HER2* probes in *HER2*-amplified tumors showed numerous clustered spots, which were detected with no apparent loss in sensitivity owing to the dye-cycling chemistry (Fig. 2J). Merger of HER2 protein and DNA FISH images allowed unambiguous comparison of DNA FISH with immunostaining of identical regions in the same sample (Fig. 2K and E).

Multiplexed Analysis of Single-Cell Mechanistic Target of Rapamycin Signaling Phenotypes in Colorectal Cancer. Using MxIF, we examined complex phenotypes of established and emerging pathological features of colorectal cancer (CRC). Sixty-one protein antigens representing multiple signal transduction pathways and cellular aspects of tumor microenvironment were stained in specimens from 747 stage I–III CRC subjects distributed on three tissue microarrays (TMAs) (Dataset S2). The experiment included 38 distinct imaging steps. Each step was conducted on a single day, including staining. Thirty-two rounds included stains and six dispersed rounds were used to acquire autofluorescence signals for image processing (Dataset S3). The region of interest for each core was recorded once before iterative staining and imaging. Subsequent imaging steps included 15 min of manual operations to set exposure times and initialize imaging, followed by automated image acquisition. Staining required about 2 h of laboratory time, including the following steps: discover-slipping (15–30 min), manual staining (1 h at room temperature), manual rinses (15 min), and manual cover-slipping (15 min). Targets included markers of hypoxia and general cell stress, common pathological markers of CRC, as well as cellular features of tumor microenvironment including immune cells,

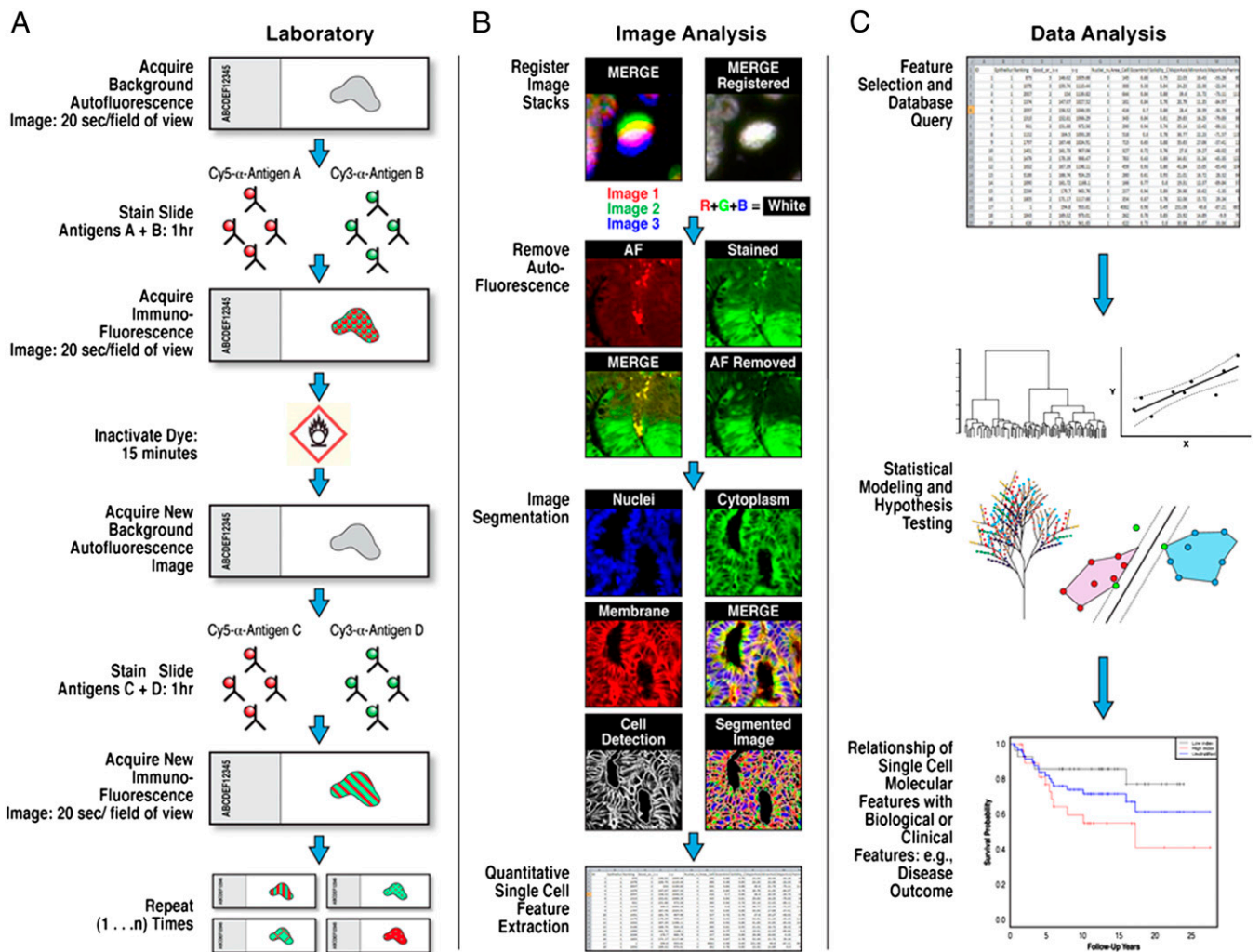


Fig. 1. MxIF data acquisition, image processing, and data analysis scheme. (A) In the laboratory, background autofluorescence (AF) tissue images are acquired before subsequent application of fluorescent dye-conjugated primary antibodies. Stained images are then acquired, followed by dye inactivation and restaining with new directly conjugated antibodies. New images are acquired, and the cycle is repeated until all target antigens are exhausted. Times associated with each step are indicated. (B) Stained images are registered, background AF is removed from each stained image, and images are segmented into epithelial and stromal regions, followed by identification of individual cells and corresponding plasma membrane, cytoplasm, and nuclear regions. Pixel-level data are summarized in cellular features, which is subsequently queried in data analysis (C). Data analysis can consist of a variety of statistical and visual explorations. In this work, we use K-median clustering to group cells with similar mTOR activity.

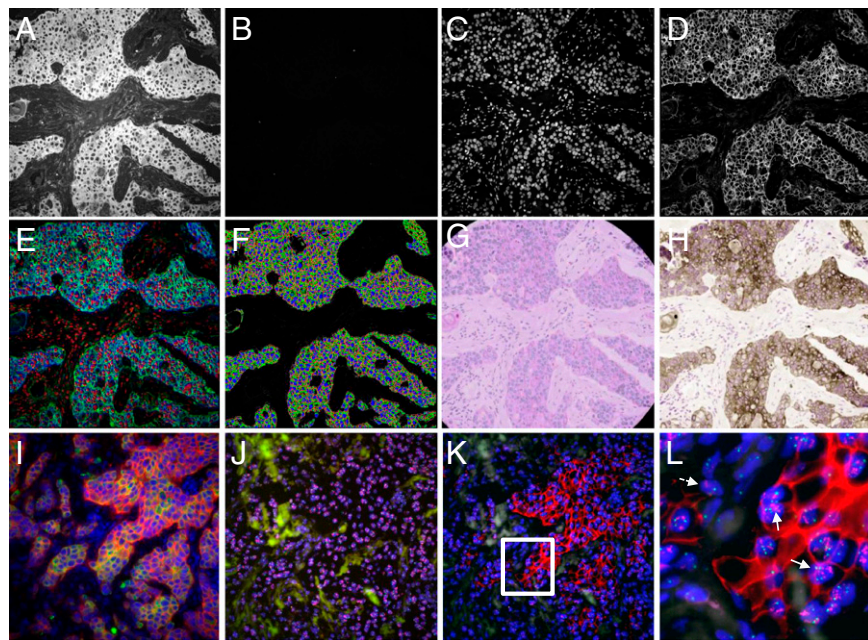
stromal cell markers, extracellular matrix, blood vasculature, and functional read-outs of several regulatory proteins and kinases (Dataset S3, Fig. 3, and Fig. S6). Positive staining of 44 antigens in a single specimen demonstrated important features of microenvironment, including endothelial cells, extracellular matrix, immune cells, fibroblasts, and additional signal transduction effectors (Fig. S6).

Kinases are important targets in the development of new anticancer therapies (19, 20). Mechanistic target of rapamycin (mTOR) is a kinase that regulates cellular growth. mTOR is dysregulated in a large proportion of human cancers and is under active clinical investigation as a therapeutic target (21, 22). Using MxIF to investigate one arm of the mTOR pathway in CRC cells, we analyzed phosphorylation levels of mTOR complex 1 (mTORC1) substrate eIF4E binding protein 1 (4E-BP1 T37/46) and ribosomal protein S6 (RPS6 S235/236), a substrate of the mTORC1 effector p70S6K (22, 23). MxIF staining of mTORC1-mediated RPS6 and 4E-BP1 phosphorylations revealed divergent signaling to 4E-BP1 and RPS6 in CRC tissues (Figs. 3 B, I and 2 and 4 C and D; Figs. S8 and S9). We expected to find positive correlations between

mTORC1-associated RPS6 and 4E-BP1 phosphorylation on a subject level and single-cell basis, but visual analysis of composite images demonstrated frequent mutual exclusivity of these modifications (Figs. 3 B, I and 2 and 4; Figs. S8 C and D and S9 A–C).

Quantitative single-cell median intensity features were used to analyze RPS6, 4E-BP1, and ERK1/2 phosphorylation in individual cells from subjects with positive staining for at least one of these markers (Dataset S3). Of the 747 subjects studied, 20 did not stain positive for ERK1/2, RPS6, or 4E-BP1 phosphorylation. Antigens representing additional physiological processes were examined in negative cases to ensure sample integrity (Fig. S10). Robust staining of at least one modified site in a minimum of 50 cells was found in 436 subjects. These subjects were analyzed further. The average number of cells analyzed in each subject was 823 (median 405, SD 972, range 51–4,700). Using K-medians clustering of whole-cell-level RPS6, 4E-BP1, and ERK1/2 phosphorylations in epithelial tumor cells, we examined clustered cell groups for patterns of staining intensity of these three modifications in all 360,082 cells that stained positive for at least one of the above phosphorylations. Consistent with our

Fig. 2. Enhanced visualization of complex tissues and MxIF coupled with DNA FISH. Breast cancer tissue was stained and analyzed by the MxIF process: (A) Cytokeratin protein staining serves as epithelial cellular marker; (B) samples are imaged to confirm dye inactivation and generate background images used in the autofluorescence removal process; (C) DAPI signal is imaged every cycle and provides a reference for image registration; and (D) Na⁺/K⁺ATPase staining serves as a membrane marker for determining cell borders. Each fluorescent channel is pseudocolored, and after registration, a merged image can be generated (E). Segmentation maps are produced for subcellular specific analysis (F). An H&E-like representation of the tissue can be generated using selective color assignment of the fluorescent signals (G). Marker stains can be viewed with chromogen-like pseudocoloring (H) including hematoxylin-like nuclear counterstain from the DAPI signal. Combined staining with dye-conjugated antibodies and DNA FISH in breast cancer tissue shows pan-keratin and HER2 protein stains together with HER2 and CEP17 FISH. Pseudocolored composite images from a representative field of view at 40× magnification are shown as follows: (I) immunofluorescence for pan-keratin (green) and Her2 (red) with DAPI (blue); (J) FISH signals for HER2 (red), CEP17 (green), and DAPI (blue); (K) Her2 immunofluorescence (red) from first imaging round overlaid with HER2 FISH (purple), CEP17 FISH (green), and DAPI (blue); and (L) magnified view of the area marked in K, highlighting Her2 amplified cells (solid arrows) showing colocalization of HER2 gene amplification and Her2 protein expression, and normal cells (dashed arrow) with normal FISH pattern and undetectable Her2 protein signal.



visual interpretation, the first division in the hierarchical clustering dendrogram of 10 K-medians cell clusters divided cells with the highest levels of RPS6 phosphorylation from those with the highest level of ERK1/2 and 4E-BP1 phosphorylation (Fig. 4A). Cluster 3:10 was the only group with above average phosphorylation of all three targets, whereas cluster 5:10 displayed robust phosphorylation of both ERK and 4E-BP1 (Fig. 4A).

Analysis of cell cluster enrichment in each subject showed that the top enriched cluster in a notable proportion of subjects displayed mutual exclusivity in signaling through one arm of the pathway in the absence of the other [RPS6 top enriched: cluster 1 (6.7%) and cluster 4 (11.6%); 4E-BP1 top enriched: cluster 5 (1.7%), cluster 2 (5%), cluster 9 (16.7%), and cluster 7 (38%)]

(Fig. 4B and Dataset S4). In contrast, only cluster 3 exhibited signaling at above average levels through both RPS6 and 4E-BP1 and was the top enriched cluster in just 2.3% of subjects analyzed (Fig. 4B and Dataset S4). These results confirm that high levels of RPS6 and 4E-BP1 phosphorylation largely occur independently at the cellular level.

RPS6 and 4E-BP1 phosphorylation were sometimes mutually exclusive in entire TMA cores representing thousands of cells from individual subjects. In subjects with cluster 2 enrichment (4E-BP1 phosphorylation high), 11/21 had zero cellular representation of robust RPS6 clusters 1, 3, and 4. Conversely, 13/50 cluster 4 enriched subjects (RPS6 phosphorylation high) are devoid of any cells from robust 4E-BP1 phosphorylation cell

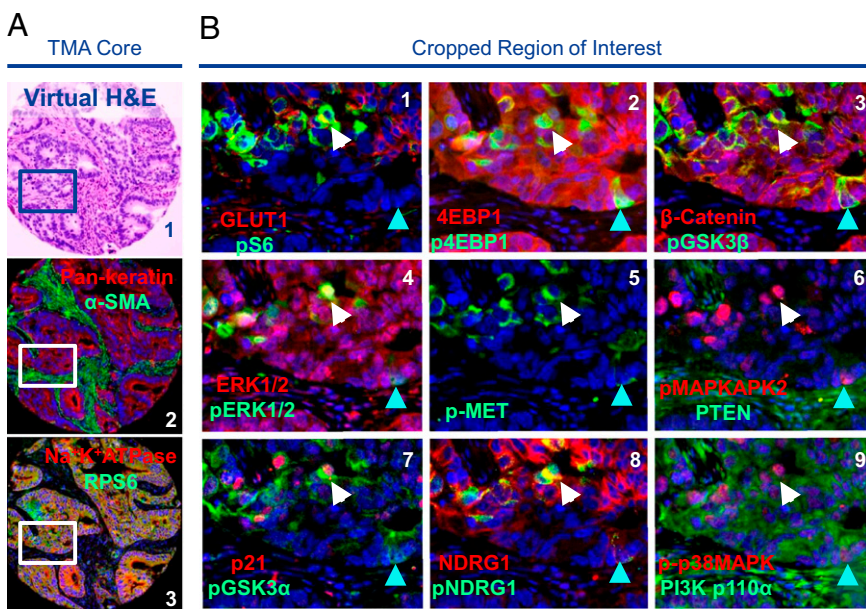


Fig. 3. Multiplexed immunofluorescence of signal transduction pathways in CRC. 747 FFPE stage I–III CRC specimens arrayed on three TMAs were stained for 61 protein antigens including markers of epithelial, immune and stromal cell lineage, subcellular compartments, oncogenes, tumor suppressors, and significant posttranslational protein modifications. Pseudocolored images of signaling and regulatory molecule staining in one small field of view are shown. Nuclei are counterstained with DAPI and pseudocolored blue in all images. (A, 1) TMA core depicted in virtual H&E. (A, 2) Pseudocolored overlaid immunofluorescence of epithelial cells stained positive for α -smooth muscle actin. (A, 3) Major subcellular compartments are detected by immunofluorescence staining of ribosomal protein S6 (cytoplasm) and Na⁺/K⁺ATPase (plasma membrane), and the nucleic acid stain DAPI (nucleus). (B) Activation of mitogenic and anabolic signaling pathways in CRC cells. Multiplexed immunofluorescence of signaling protein expression and phosphorylation shows complex activation and repression patterns of regulatory and signal transduction pathways. The white arrow indicates a single cell expressing each feature and the cyan arrow indicates a cell with differential expression of features.

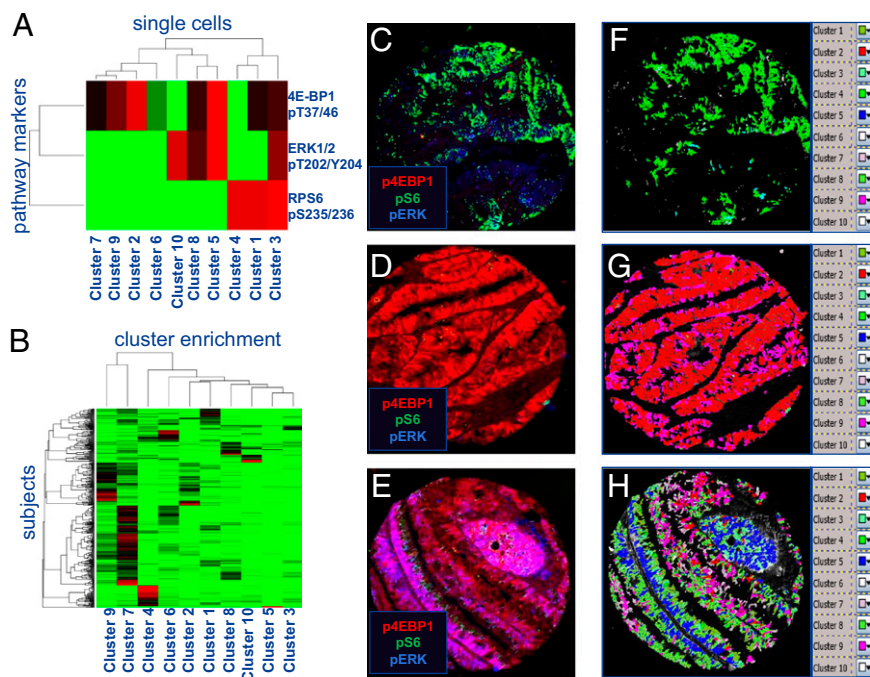


Fig. 4. Cluster analysis shows large-scale divergence of signaling to RPS6, 4E-BP1, and ERK1/2 in CRC cells. (A) K-medians clustering heat map of 4E-BP1 pThr37/46, RPS6 pSer 235/236, and ERK1/2 pT202/Y204 staining in 3.6×10^5 CRC cells from 720 subjects (abbreviated as p4EBP1, pS6, and pERK). (B) K-medians clustering heat map of enrichment in clusters from A in 436 subjects with ≥ 50 cells positive for p4E-BP1, pS6, or pERK. (C–E) Pseudocolor overlaid images of representative subjects enriched for mutually exclusive subject-level signaling (C and D) and a subject with many cell clusters (E) are shown. Mapping of cell clusters back on to images demonstrates cases exhibiting homogeneity (F and G) or heterogeneity (H) of cluster assignment. The legends in F–H show the colors selected to represent each cluster.

clusters, and 40/50 cluster 4 enriched subjects shared fewer than 5% of cells from any of the clusters with robust activation of 4E-BP1 (clusters 2, 3, 5, and 9) (Fig. 4A and B and Dataset S4).

Because ribosomal S6 protein kinase (p90RSK) has been shown to phosphorylate RPS6 in an ERK1/2-dependent manner, we asked whether clusters with high levels of RPS6 phosphorylation were associated with high levels of activated ERK1/2 modifications at the single-cell level (24). In three of four cell clusters with above-average ERK1/2 phosphorylation, average RPS6 phosphorylation was negative, whereas cluster 3 was associated with high levels of RPS6 phosphorylation (Figs. 3 and 4A and B and Fig. S9). However, cluster 3 was inconsistent with an exclusively mTORC1-independent, p90RSK-mediated RPS6 phosphorylation mechanism because it also exhibits above-average phosphorylation of 4E-BP1 (Fig. 4A). Further examination of the degree to which cell clusters with high levels of ERK1/2 activation coincide with the occurrence of clusters with high levels of RPS6 and 4E-BP1 phosphorylation at the subject level revealed little overlap between these clusters in the tumor regions analyzed (Fig. 4B). Taken together, these results suggest mTORC1 usually signals to these molecules under distinct spatiotemporal conditions in CRC cells, *in vivo*.

Discussion

In this work, we show that MxIF enables high-order, multiplexed, *in situ* microscopic analysis of biological molecules in individual cells. Although our applications focus on cancer, MxIF readily extends to tissue or cellular imaging research outside of oncology and should benefit many disciplines of basic and translational research and ultimately affect clinical practice.

Several limitations of current multiplexed fluorescence microscopy imaging technologies are overcome by MxIF. Attempting to catalog quantitative colocalized molecular features of cells with standard immunofluorescence methods becomes increasingly unfeasible as the number of analytes increases (e.g., to achieve all possible combinations of pairwise immunofluorescence of 61 proteins would require a prohibitive 1,830 samples). We detected 61 different protein epitopes in single FFPE tissue sections. An upper limit of analytes that can be examined in a single MxIF assay has not been reached. We also integrated MxIF with DNA FISH and H&E stains.

Our automated image analysis algorithms enable analysis of high-complexity cellular image data. Segmentation of tissue images into specific cell types and subcellular compartments facilitates quantitative subcellular biomarker localization measurements that agree with manual interpretation (Figs. S11 and S12). The repeated imaging of DAPI-stained nuclei provides fiducial points for each multiplexing round, allowing our registration algorithms to achieve accurate alignment of sequentially acquired images, which is vital to pixel-level analysis of molecular colocalization. We also developed algorithms to perform field flattening, autofluorescence removal, and regional, cellular, and subcellular quantitation of protein expression.

Alternative multiplexed microscopy strategies have been reported by others. Multiplexed imaging has been demonstrated by eluting or stripping antibodies with low pH or denaturation (25–27). Multiepitope ligand cartography (MELC) is a photobleaching technique to achieve dye cycling (28–30). The process has demonstrated imaging of 100 antigens in a single sample. Although MELC data allow analysis of protein networks within tissues, accompanying subcellular quantitation and integration with histological stains and DNA FISH have not been reported. Like the MELC approach, steric hindrance is generally not observed in our sequential antibody staining.

MxIF study of CRC allowed the mapping of cellular mTORC1 and MAPK signal transduction patterns in tissues with unprecedented resolution. Cluster analysis reveals that high-level phosphorylation of mTORC1-associated targets 4E-BP1 and RPS6 rarely occurs in the same cell, more often occurring in mutual exclusivity of one another. This likely reflects temporal or functional variation in mTORC1 signaling to these molecules, or cross-talk with other signaling pathways (Fig. S9 and Dataset S4). Taken together with the finding that MAPK signaling known to be upstream of RPS6 phosphorylation is rarely found in cells and subjects with robust phospho-RPS6^{high}/phospho-4E-BP1^{low} phenotypes, our data suggest contextually distinct mechanisms regulating mTORC1 signaling to these canonical downstream targets in human colorectal tumors (Fig. 4 and Figs. S6 and S9). In line with these findings, emerging experimental models of mTOR signaling suggest that cells differentially regulate canonical processes downstream of mTORC1. Recent work dissecting mTOR

function by genetic and pharmacological means shows that mTORC1 signaling through established targets S6K1 and 4E-BP1 can be regulated in distinct manners and influence different cellular functions (31). Rapamycin fails to inhibit mTORC1-mediated 4E-BP1 phosphorylation in many contexts, suggesting mTORC1 uses discrete mechanisms or binding partners to interact with its substrates (32). Our findings should be examined in model systems to better understand the functional significance of these divergences.

Our method combines data from morphological, protein, and DNA FISH-based analyses using a single sample. Automated segmentation and quantitation of fluorescence images enables standardization and assay robustness. The preservation of sample integrity and the combination of H&E imaging with molecular marker information maximizes molecular data from limited sample resources. Single-cell and subcellular analysis and cell clustering algorithms allowed identification of clusters that were relatively rare in the overall population (range 1.2–16.4%), demonstrating the utility of this approach in finding rare cell phenotypes such as transient signaling events. Furthermore, this platform allows characterization of additional features of interest

such as cancer stem cells and tumor microenvironment, enabling high-content analysis of human tissues and extending established high-throughput in vitro cellular imaging methods.

Materials and Methods

Descriptions of additional results are included in *SI Results*. Specimens were acquired in adherence to institutional guidelines, Reagents, fluorescence microscopy hardware, immunofluorescence and FISH techniques, image processing, image and data analysis, antibody conjugation chemistry, and dye inactivation procedures are given in *SI Materials and Methods*.

ACKNOWLEDGMENTS. We graciously acknowledge the late Dr. William Gerald for providing valuable insight into tissue-based biomarker detection and the tissue arrays and stained slides for the pathologist's comparison study. We also thank Brian Ring (Clariant Inc.) and Rodney Beck, Douglass T. Ross, and Robert Seitz (formerly of Clariant Inc.), for providing colorectal cancer TMAs. Additionally, we acknowledge funding support, valuable discussions, and scientific input during the development of this work from Anirban Bhaduri, Christoph Hergersberg, John Burczak, Tom Treynor, Maureen Breshnahan, Jenifer Haeckl, and Dileep Vangasseri; and thank Tricia Tanner for significant editorial support during the manuscript writing process.

1. Anonymous; Cancer Genome Atlas Network (2012) Comprehensive molecular portraits of human breast tumours. *Nature* 490(7418):61–70.
2. Sorlie T, et al. (2001) Gene expression patterns of breast carcinomas distinguish tumor subclasses with clinical implications. *Proc Natl Acad Sci USA* 98(19):10869–10874.
3. Anonymous; Cancer Genome Atlas Research Network (2011) Integrated genomic analyses of ovarian carcinoma. *Nature* 474(7353):609–615.
4. Kwan ML, et al. (2009) Epidemiology of breast cancer subtypes in two prospective cohort studies of breast cancer survivors. *Breast Cancer Res* 11(3):R31.
5. Verhaak RG, et al.; Cancer Genome Atlas Research Network (2010) Integrated genomic analysis identifies clinically relevant subtypes of glioblastoma characterized by abnormalities in PDGFRA, IDH1, EGFR, and NF1. *Cancer Cell* 17(1):98–110.
6. Hammerman PS, et al.; Cancer Genome Atlas Research Network (2012) Comprehensive genomic characterization of squamous cell lung cancers. *Nature* 489(7417):519–525.
7. Butcher EC, Berg EL, Kunkel EJ (2004) Systems biology in drug discovery. *Nat Biotechnol* 22(10):1253–1259.
8. Ring BZ, et al. (2006) Novel prognostic immunohistochemical biomarker panel for estrogen receptor-positive breast cancer. *J Clin Oncol* 24(19):3039–3047.
9. Ring BZ, et al. (2009) A novel five-antibody immunohistochemical test for subclassification of lung carcinoma. *Mod Pathol* 22(8):1032–1043.
10. Ross DT, et al. (2008) Chemosensitivity and stratification by a five monoclonal antibody immunohistochemistry test in the NSABP B14 and B20 trials. *Clin Cancer Res* 14(20):6602–6609.
11. Rimm DL (2006) What brown cannot do for you. *Nat Biotechnol* 24(8):914–916.
12. Tsurui H, et al. (2000) Seven-color fluorescence imaging of tissue samples based on Fourier spectroscopy and singular value decomposition. *J Histochem Cytochem* 48(5):653–662.
13. Monici M (2005) Cell and tissue autofluorescence research and diagnostic applications. *Biotechnol Annu Rev* 11:227–256.
14. Gerdes MJ, et al. (2010) Sequential analysis of biological samples. US Patent: 7 741 045, issued June 22, 2010.
15. Gerdes MJ, Sood A, Sevinsky CJ (2011) Method and apparatus for antigen retrieval process. US Patent: 8 067 241, issued November 29, 2011.
16. Ginty F, et al. (2008) The relative distribution of membranous and cytoplasmic met is a prognostic indicator in stage I and II colon cancer. *Clin Cancer Res* 14(12):3814–3822.
17. Bello M, Tao X, Can A (2008) Accurate registration and failure detection in tissue micro array images. *Proceedings of the 2008 IEEE International Symposium on Biomedical Imaging: From Nano to Macro* (Inst Electrical Electronics Engineers, New York), pp 368–371.
18. Nitta H, et al. (2012) A gene-protein assay for human epidermal growth factor receptor 2 (HER2): Brightfield tricolor visualization of HER2 protein, the HER2 gene, and chromosome 17 centromere (CEN17) in formalin-fixed, paraffin-embedded breast cancer tissue sections. *Diagn Pathol* 7(1):60.
19. Jänne PA, Gray N, Settleman J (2009) Factors underlying sensitivity of cancers to small-molecule kinase inhibitors. *Nat Rev Drug Discov* 8(9):709–723.
20. Dar AC, Shokat KM (2011) The evolution of protein kinase inhibitors from antagonists to agonists of cellular signaling. *Annu Rev Biochem* 80:769–795.
21. Ma XM, Blenis J (2009) Molecular mechanisms of mTOR-mediated translational control. *Nat Rev Mol Cell Biol* 10(5):307–318.
22. Graff JR, et al. (2007) Therapeutic suppression of translation initiation factor eIF4E expression reduces tumor growth without toxicity. *J Clin Invest* 117(9):2638–2648.
23. Graff JR, et al. (2009) eIF4E activation is commonly elevated in advanced human prostate cancers and significantly related to reduced patient survival. *Cancer Res* 69(9):3866–3873.
24. Roux PP, et al. (2007) RAS/ERK signaling promotes site-specific ribosomal protein S6 phosphorylation via RSK and stimulates cap-dependent translation. *J Biol Chem* 282(19):14056–14064.
25. Glass G, Papin JA, Mandell JW (2009) SIMPLE: A sequential immunoperoxidase labeling and erasing method. *J Histochem Cytochem* 57(10):899–905.
26. Pirici D, et al. (2009) Antibody elution method for multiple immunohistochemistry on primary antibodies raised in the same species and of the same subtype. *J Histochem Cytochem* 57(6):567–575.
27. Wählby C, Erlandsson F, Bengtsson E, Zetterberg A (2002) Sequential immunofluorescence staining and image analysis for detection of large numbers of antigens in individual cell nuclei. *Cytometry* 47(1):32–41.
28. Friedenberger M, Bode M, Krusche A, Schubert W (2007) Fluorescence detection of protein clusters in individual cells and tissue sections by using topomere imaging system: sample preparation and measuring procedures. *Nat Protoc* 2(9):2285–2294.
29. Schubert W, et al. (2006) Analyzing proteome topology and function by automated multidimensional fluorescence microscopy. *Nat Biotechnol* 24(10):1270–1278.
30. Schubert W, Gieseler A, Krusche A, Hillert R (2009) Topomere mapping in prostate cancer: Detection of 2000 cell surface protein clusters in a single tissue section and cell type specific annotation by using a three symbol code. *J Proteome Res* 8(6):2696–2707.
31. Hsieh AC, et al. (2010) Genetic dissection of the oncogenic mTOR pathway reveals druggable addiction to translational control via 4EBP-eIF4E. *Cancer Cell* 17(3):249–261.
32. Choo AY, Yoon SO, Kim SG, Roux PP, Blenis J (2008) Rapamycin differentially inhibits S6Ks and 4E-BP1 to mediate cell-type-specific repression of mRNA translation. *Proc Natl Acad Sci USA* 105(45):17414–17419.